

# Scalable and Flexible Deep Bayesian Optimization with Auxiliary Information for Scientific Problems

Samuel Kim<sup>1</sup> Peter Y. Lu<sup>2</sup> Charlotte Loh<sup>1</sup> Jamie Smith<sup>3</sup> Jasper Snoek<sup>3</sup> Marin Soljačić<sup>2</sup>

## Abstract

Bayesian optimization (BO) is a popular paradigm for global optimization of expensive black-box functions, but there are many domains where the function is not completely black-box. The data may have some known structure, e.g. symmetries, and the data generation process can yield useful intermediate or auxiliary information in addition to the value of the optimization objective. However, surrogate models traditionally employed in BO, such as Gaussian Processes (GPs), scale poorly with dataset size and struggle to incorporate known structure or auxiliary information. Instead, we propose performing BO on complex, structured problems by using Bayesian Neural Networks (BNNs), a class of scalable surrogate models that have the representation power and flexibility to handle structured data and exploit auxiliary information. We demonstrate BO on a number of realistic problems in physics and chemistry, including topology optimization of photonic crystal materials using convolutional neural networks, and chemical property optimization of molecules using graph neural networks. On these complex tasks, we show that BNNs often outperform GPs as surrogate models for BO in terms of both sampling efficiency and computational cost.

## 1. Introduction

Bayesian optimization (BO) is a global optimization algorithm well-suited for expensive, black-box, derivative-free functions and has been successfully applied to a wide range of problems in science and engineering (Ueno et al., 2016; Griffiths & Hernández-Lobato, 2020; Korovina et al., 2020)

<sup>1</sup>Department of Electrical Engineering and Computer Science, Massachusetts Institute of Technology, Cambridge, Massachusetts, USA <sup>2</sup>Department of Physics, Massachusetts Institute of Technology, Cambridge, Massachusetts, USA <sup>3</sup>Google Research, Cambridge, Massachusetts, USA. Correspondence to: Samuel Kim <samkim@mit.edu>.

as well as hyperparameter tuning of machine learning models (Snoek et al., 2012; Swersky et al., 2014; Klein et al., 2017). By training a Bayesian surrogate model on the available data, BO can efficiently decide the next data point to label in each iteration to maximize sampling efficiency.

However, in many domains, the objective function is not a complete black box. Many complex, high-dimensional input spaces such as images or molecules have some known structure or symmetries. In addition, rather than directly outputting the value of the objective, the data collection process may instead provide intermediate or auxiliary information from which the objective function can be cheaply computed. For example, a scientific experiment or simulation may produce multiple measurements, such as the optical scattering spectrum of a nanoparticle over a range of wavelengths or the multiple quantum chemistry properties of a molecule from a single density functional theory (DFT) calculation. These are important factors for designing and training an accurate surrogate model, but they are often not fully exploited in existing methods and applications.

Typically the surrogate model in BO is a Gaussian Process (GP), as the posterior predictive distribution can be expressed analytically. However, (1) inference in GPs scales cubically with the number of observations and output dimensionality, limiting its use with larger datasets, and (2) GPs operate most naturally over continuous spaces, and so kernels for high-dimensional data with complex structure must be carefully formulated and tuned by hand for each new task. Encoding inductive biases, symmetries, and invariances can be challenging. Random forests have also been used for iterative optimization as they do not face scaling challenges; however, they still face the same issues with encoding complex structures (Hutter et al., 2011).

More recently, Bayesian neural networks (BNNs) have been proposed as surrogate models for BO since BNNs can be efficiently trained on extremely large datasets (Snoek et al., 2015; Springenberg et al., 2016). Additionally, the ability to incorporate a variety of constraints, symmetries, and inductive biases into BNN architectures allows BO to be applied to more complex tasks with structured data.

This work aims to further expand upon the use of BNNs

as surrogate models in BO and apply BO to real-world scientific datasets. Our contributions are as follows:

- We take advantage of auxiliary information to improve BNN-based BO for tasks with high-dimensional observations
- We demonstrate BO on complex input spaces including images and molecules using convolutional and graph neural networks, respectively.
- We apply BO to several realistic scientific datasets, including the optical scattering of a nanoparticle, topology optimization of a photonic crystal material, and chemical property optimization of molecules from the QM9 dataset.

We focus on scientific problems both because the applications are important and because these tasks serve as a useful and challenging testing ground. We show that BNNs are often able to significantly outperform GPs on these problems, and we believe that these strong results will also generalize to other contexts and enable BO to be applied to a wider range of problems.

We make our datasets and code publicly available at <http://github.com/placeholder/deepBO>.

## 2. Related Work

Bayesian optimization of problems with intermediate representations have been studied on synthetic problems that have been decomposed into composite functions (Astudillo & Frazier, 2019). However, the multi-output GP they use scales poorly with output dimensionality, and so is limited to simpler problems. Additionally, GP kernels have been formulated for complex input spaces including convolutional kernels (Van der Wilk et al., 2017; Novak et al., 2020; Wilson et al., 2016) and graph kernels (Shervashidze et al., 2011; Walker & Glocker, 2019).

Neural networks have been previously integrated into a surrogate model for BO by using them as an adaptive basis function for Bayesian linear regression (Snoek et al., 2015). Perrone et al. (2018) showed how this can enable BO in more complex settings, including transfer learning of the adaptive basis across multiple tasks, and modeling of auxiliary signals to improve performance. Alternatively, BNNs that use Hamiltonian Monte Carlo to sample the posterior have been used for single-task and multi-task BO for hyperparameter optimization (Springenberg et al., 2016).

Active learning is a similar scheme to BO that, instead of optimizing an objective function, aims to optimize the predictive ability of a model with as few data points as possible. Deep learning has enabled active learning on a variety of high-dimensional data including images (Gal et al., 2017), language (Siddhant & Lipton, 2018), and partial differential

equations (Zhang et al., 2019a). BNNs have also been applied in another similar setting, contextual bandits, where the model chooses between discrete actions to maximize expected reward (Blundell et al., 2015; Riquelme et al., 2018).

## 3. Bayesian Optimization

We formulate BO as a maximization problem in which we wish to find  $\mathbf{x}^* \in \mathcal{X}, y^* = f(\mathbf{x}^*) \in \mathcal{Y}$  such that  $\mathbf{x}^* = \arg \max_{\mathbf{x}} f(\mathbf{x})$ . In general,  $f$  can be a noisy function, but here we assume that evaluations are noise-free, which is typical for numerical simulations in many fields of science.

We briefly review the BO algorithm here, and more details can be found in the Supplementary Materials and in the literature (Brochu et al., 2010; Shahriari et al., 2015). In each iteration, a surrogate model  $\mathcal{M}$  is trained on a labeled dataset  $\mathcal{D}_{\text{train}} = \{(\mathbf{x}_n, y_n)\}_{n=1}^N$ , where  $\mathcal{M}$  provides a prediction probability distribution that represent predictive uncertainty. An acquisition function  $\alpha$  then uses  $\mathcal{M}$  to suggest the next data point  $\mathbf{x}_{N+1} \in \mathcal{X}$  to label, where

$$\mathbf{x}_{N+1} = \arg \max_{\mathbf{x} \in \mathcal{X}} \alpha(\mathbf{x}; \mathcal{M}, \mathcal{D}_{\text{train}}). \quad (1)$$

The new data is evaluated to get  $y_{N+1} = f(\mathbf{x}_{N+1})$ , and  $(\mathbf{x}_{N+1}, y_{N+1})$  is added to  $\mathcal{D}_{\text{train}}$ . The optimization continues until some stopping criteria is met.

### 3.1. Continued Training with Learning Rate Annealing

One challenge is that training  $\mathcal{M}$  on  $\mathcal{D}_{\text{train}}$  from scratch in every optimization loop adds a large computational cost that limits the applicability of our algorithm. This is especially true in the case where BNNs are used for  $\mathcal{M}$ , which are ideally trained for a long time until convergence.

To minimize the training time in each optimization loop, we use the model that has been trained in the  $N$ th optimization loop iteration as the initialization (also known as a “warm start”) for the  $(N + 1)$ th iteration, rather than training from a random initialization. This enables the model’s training loss to converge in only a few epochs. However, we have found that naive continued training results in poor BO performance because training does not converge for the new data point  $\mathcal{D}_{\text{new}} = (\mathbf{x}_{N+1}, y_{N+1})$  relative to the rest of the data under a limited computational budget, resulting in the acquisition function possibly labeling similar points in consecutive iterations. To mitigate this, we use the cosine annealing learning rate proposed in Loshchilov & Hutter (2016) which starts with a large learning rate and drops the learning rate to 0. This also has the advantage of allowing the model to more easily explore a multimodal posterior (Huang et al., 2017).

### 3.2. Acquisition Function

We choose the expected improvement (EI) acquisition function  $\alpha_{\text{EI}}$  (Jones et al., 1998). When the prediction distribution from the surrogate model  $\mathcal{M}$  is a normal distribution  $\mathcal{N}(\mu(\mathbf{x}), \sigma^2(\mathbf{x}))$ , EI can be expressed analytically as

$$\alpha_{\text{EI}}(\mathbf{x}) = \sigma(\mathbf{x})[\gamma(\mathbf{x})\Phi(\gamma(\mathbf{x})) + \phi(\gamma(\mathbf{x}))], \quad (2)$$

where  $\gamma(\mathbf{x}) = (\mu(\mathbf{x}) - y_{\text{best}})/\sigma(\mathbf{x})$ ,  $y_{\text{best}} = \max(\{y_n\}_{n=1}^N)$  is the best value of the objective function so far, and  $\phi$  and  $\Phi$  are the PDF and CDF of the standard normal  $\mathcal{N}(0, 1)$ , respectively. For surrogate models that do not give an analytical form for the prediction distribution, we sample from the posterior  $N_{\text{MC}}$  times and use a Monte Carlo approximation of EI:

$$\alpha_{\text{EI-MC}}(\mathbf{x}) = \frac{1}{N_{\text{MC}}} \sum_{i=1}^{N_{\text{MC}}} \max(\mu^{(i)}(\mathbf{x}) - y_{\text{best}}, 0). \quad (3)$$

where  $\mu^{(i)}$  is a prediction sampled from the posterior of  $\mathcal{M}$ . Unless otherwise stated, we set  $N_{\text{MC}} = 30$  and choose the next data point to label by maximizing EI on a pool of  $|\mathcal{X}_{\text{pool}}| = 10^5$  randomly sampled points.

### 3.3. Auxiliary Information

Typically we assume  $f$  is a black box function, so we train  $\mathcal{M}: \mathcal{X} \rightarrow \mathcal{Y}$  to model  $f$ . Here we consider the case where the experiment or observation may provide some intermediate or auxiliary information  $\mathbf{z} \in \mathcal{Z}$ , such that  $f$  can be decomposed as

$$f(\mathbf{x}) = h(g(\mathbf{x})), \quad (4)$$

where  $g: \mathcal{X} \rightarrow \mathcal{Z}$  is the expensive labeling process, and  $h: \mathcal{Z} \rightarrow \mathcal{Y}$  is a known objective function that can be cheaply computed. In this case, we train  $\mathcal{M}: \mathcal{X} \rightarrow \mathcal{Z}$  to model  $g$ , and the approximate EI acquisition function becomes

$$\alpha_{\text{EI-MC-aux}}(\mathbf{x}) = \frac{1}{N_{\text{MC}}} \sum_{i=1}^{N_{\text{MC}}} \max(h(\mu^{(i)}(\mathbf{x})) - y_{\text{best}}, 0). \quad (5)$$

We denote models trained using auxiliary information with the suffix “-aux.”

## 4. Surrogate Models

**Ensembles** Lakshminarayanan et al. (2017) suggest ensembling neural networks that directly predict both the mean and variance to allow for heteroscedastic noise. In contrast, we assume noise-free labels (which is common for scientific numerical simulations) and use the variance across the ensemble to build the prediction distribution rather than directly parameterizing the variance. Our ensemble size is  $N_{\text{MC}} = 10$ .

**Variational BNNs** We use Bayes by Backprop (BBB), a variational method that approximates the posterior over the neural network weights with independent normal distributions (Blundell et al., 2015). We also compare Multiplicative Normalizing Flows (MNF) in the Supplementary Material, which uses normalizing flows for more expressive posterior distributions (Louizos & Welling, 2017).

**Neural Linear Models** We use a neural network as an adaptive basis for Bayesian linear regression (Snoek et al., 2015).

**Infinite-Width Neural Networks** We implement infinite-width neural networks using the Neural Tangents library (Novak et al., 2020).

**GP Baselines** We implement BO using Gaussian Processes (GPs) with a Matérn kernel using the GPyOpt library (The GPyOpt authors, 2016). The library optimizes over the acquisition function in the inner loop using the L-BFGS algorithm. We also implement GPs using various kernels provided by the Neural Tangents library, including convolutional kernels for images (Novak et al., 2020). Additionally, we compare against BO with multi-output GPs (MOGPs) for composite functions as implemented by Astudillo & Frazier (2019).

**Other Baselines** We compare against several global optimization algorithms that do not use Bayesian surrogate models and are cheap to run. LIPO (Malherbe & Vayatis, 2017) is implemented in the dlib library (King, 2009). DIRECT-L (Gablonsky & Kelley, 2001) is implemented in the NLOpt library (Johnson, 2010). CMA-ES is implemented in the pycma library (Hansen et al., 2019).

Ensembles and variational methods can easily scale up to high-dimensional outputs with minimal increase in computational cost by simply changing the output layer size, and so we can use the “-aux” variants of these architectures in BO. Neural Linear and GPs scale cubically with output dimensionality, making them infeasible to train on high-dimensional auxiliary information.

## 5. Experiments

We first examined small-scale, low-dimensional problems without auxiliary or structural information, namely the Branin and Hartmann-6 functions, and found that GPs performed the best as expected. Notably, BNNs are competitive with GPs, showing that they are viable even for these simple problems. These results can be found in the supplementary.

We now look at three scientific optimization tasks all of which provide auxiliary information that can be leveraged. These tasks are more difficult than the synthetic tasks typically studied. In the latter two tasks, the structure of the data also becomes important and hence BNNs significantly outperform GPs and other baselines. Due to space constraints,

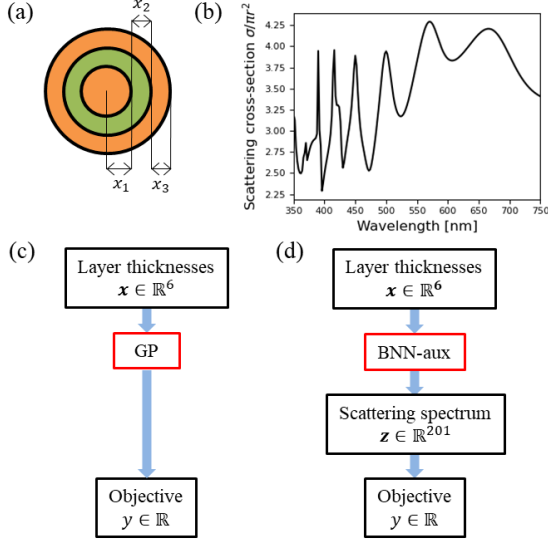


Figure 1. (a) A three-layer nanoparticle parameterized by the layer thicknesses. (b) An example of the scattering cross-section spectrum of a six-layer nanoparticle. (c) Whereas GPs are trained to directly predict the objective function, (d) multi-output BNNs can be trained with auxiliary information, which here is the scattering spectrum.

we only highlight results from select architectures (see Supplementary Materials for full results along with dataset and hyperparameter details). All BO results are averaged over multiple trials, and the shaded area in the plots represents  $\pm$  one standard error over the trials.

### 5.1. Multilayer Nanoparticle

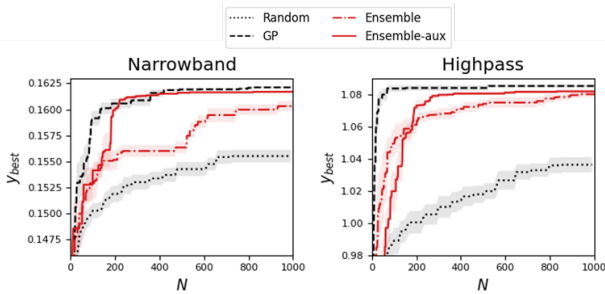


Figure 2. BO results for two different objective functions for the nanoparticle scattering problem. Training with auxiliary information (where  $\mathcal{M}$  is trained to predict  $\mathbf{z}$ ) is denoted with “aux”. Adding auxiliary information to BNNs significantly improves performance.

Our first real-world optimization task looks at a simple domain in which we can observe the effect of providing auxiliary information to BNNs in BO. We consider the problem of light scattering from a multilayer nanoparticle which

consists of a lossless silica core and 5 shells of alternating  $\text{TiO}_2$  and silica. The particle is parameterized by the core radius and layer thicknesses as shown in Figure 1(a), which we restrict to the range 30 nm to 70 nm. Because the size of the nanoparticle is on the order of the wavelength of light, its optical properties can be tuned by the number and thicknesses of the layers. These particles have a wide variety of applications that demand a tailored optical response (Ghosh Chaudhuri & Paria, 2012) including biological imaging (Saltsberger et al., 2012), improved solar cell efficiency (Ho et al., 2012; Shi et al., 2013), and catalytic materials (Tang & Henkelman, 2009).

We wish to optimize the scattering cross-section spectrum over a range of visible wavelengths, an example of which is shown in Figure 1(b). In particular, we compare two different objective functions: the narrowband objective that aims to maximize scattering in the small range 600 nm to 640 nm and minimize it elsewhere, and the highpass objective that aims to maximize scattering above 600 nm and minimize it elsewhere. While GPs train directly on the objective function, BNNs can be trained to predict the full scattering spectrum, i.e. the auxiliary information  $\mathbf{z} \in \mathbb{R}^{201}$ , which is then used to calculate the objective function, as shown in Figure 1(c,d).

BO results are shown in Table 1, and select results are plotted in Figure 2. Adding auxiliary information significantly improves BO performance for both ensembles and BBB. Additionally, they are competitive with GPs, making BNNs a viable approach for scaling BO to large datasets. Surprisingly, the infinite ensemble of infinite-width networks performs poorly compared to normal ensembles, suggesting that the infinite-width formulations do not fully capture the dynamics of their finite-width counterparts. We also compare to MOGPs in the supplemental information. Due to the poor scaling of MOGPs with respect to output dimensionality, we could only run MOGPs for 50 iterations in a comparable amount of time. Even within 50 iterations, MOGPs perform poorly, comparable to random sampling.

### 5.2. Photonic Crystal Topology

Next we look at a more complex, high-dimensional domain that contains symmetries not easily exploitable by GPs. Photonic crystals (PCs) are nanostructured materials that are engineered to exhibit exotic optical properties not found in bulk materials, including photonic band gaps, negative index of refraction, and angular selective transparency (John, 1987; Yablonovitch, 1987; Joannopoulos et al., 2008; Shen et al., 2014). As advanced fabrication techniques are enabling smaller and smaller feature sizes, there has been growing interest in inverse design and topology optimization to design even more sophisticated PCs (Jensen & Sigmund, 2011; Men et al., 2014) for applications in photonic inte-



Table 1. Select BO results for the nanoparticle scattering problem. “-AUX” refers to models trained with auxiliary information. “INF” refers to infinite ensemble of infinite-width NNs, trained with continuous gradient descent for infinite time, with “NNGP” and “NTK” being the choice of kernel.

MODEL	NARROWBAND				HIGHPASS			
	$y_{\text{BEST}}$ AT $N = 250$		$y_{\text{BEST}}$ AT $N = 1000$		$y_{\text{BEST}}$ AT $N = 250$		$y_{\text{BEST}}$ AT $N = 100$	
	MEAN	SE	MEAN	SE	MEAN	SE	MEAN	SE
GP	0.1606	0.0005	0.1621	0.0001	1.0839	0.0017	1.0851	0.0008
ENSEMBLE	0.1558	0.0011	0.1607	0.0003	1.0729	0.0025	1.077	0.0021
ENSEMBLE-AUX	0.1578	0.0014	0.1593	0.0013	1.0783	0.0003	1.0822	0.001
BBB	0.1596	0.0006	0.1596	0.0006	1.0753	0.0005	1.0753	0.0005
BBB-AUX	0.1601	0.001	0.1601	0.001	1.076	0.0028	1.076	0.0028
NEURAL LINEAR	0.1543	0.002	0.1579	0.0015	1.0798	0.0007	1.0836	0.0007
INF-NNGP-STD	0.1551	0.0006	0.1598	0.0006	1.0615	0.0043	1.069	0.0018
INF-NTK-STD	0.1564	0.0006	0.1607	0.0001	1.0607	0.0039	1.0761	0.0014
RANDOM	0.1527	0.0008	0.1555	0.0006	1.0053	0.0063	1.0362	0.0047
LIPO	0.1604	0.0016	0.1619	0.0006	1.0792	0.0066	1.087	0.0034
DIRECT-L	0.1544	0	0.156	0	1.0777	0	1.0801	0

grated circuits, flat lenses, and sensors (Piggott et al., 2015; Lin et al., 2019).

Here we consider 2D PCs consisting of periodic unit cells represented by a  $32 \times 32$  pixel image, as shown in figure 3(a), with white and black regions representing vacuum (or air) and silicon, respectively. Because optimizing over raw pixel values may lead to pixel-sized features or intermediate pixel values that cannot be fabricated, we have parameterized the PCs with a level-set function  $\phi: \mathcal{X} \rightarrow \mathcal{V}$  that converts a 51-dimensional feature vector  $\mathbf{x} = [c_1, c_2, \dots, c_{50}, \Delta] \in \mathbb{R}^{51}$  representing the level-set parameters into an image  $\mathbf{v} \in \mathbb{R}^{32 \times 32}$  that represents the PC.

We test BO on two different data distributions, which are shown in Figure 3(b,c). In the PC-A distribution,  $\mathbf{x}$  spans  $c_i \in [-1, 1], \Delta \in [-3, 3]$ . In the PC-B distribution, we arbitrarily restrict the domain to  $c_i \in [0, 1]$ . The PC-A data distribution is translation invariant, meaning that any PC with a translational shift will also be in the data distribution. However, the PC-B data distribution is not translation invariant, as shown by the white regions in the center of all the examples in Figure 3(c). The optical properties of PCs can be characterized by their photonic density of states (DOS), e.g. see Figure 3(d). We choose an objective function that aims to minimize the DOS in a certain frequency range while maximizing it everywhere else, which corresponds to opening up a photonic band gap in said frequency range.

As shown in Figure 3(e,f), we train GPs directly on the level-set parameters  $\mathcal{X}$ , whereas we train the Bayesian convolutional NNs (BCNNs) on the more natural unit cell image space  $\mathcal{V}$ . BCNNs can also be trained to predict the full DOS as auxiliary information  $\mathbf{z} \in \mathbb{R}^{500}$ . The BO results, seen in Figure 4, show that BCNNs outperform GPs by a significant margin on both datasets, which is due to both the auxiliary information and the inductive bias of the convolutional

layers, as shown in Figure 5(a). Because the behavior of PCs is determined by their topology rather than individual pixel values, BCNNs are much better suited to analyze this dataset as opposed to GPs. Additionally, BCNNs can be made much more data-efficient since they directly encode translation invariance and thus learn the behavior of a whole class of translated images from a single image.

For our main experiments with BCNNs, we use an architecture that respects translation invariance. To demonstrate the effect of another commonly used deep learning training technique, we also experiment with incorporating translation invariance into a translation dependent (i.e. *not* translation invariant) architecture using a data augmentation scheme in which each image is randomly translated, flipped, and rotated during training. We expect data augmentation to improve performance when the data distribution exhibits the corresponding symmetries: in this case, we focus on translation invariance. As shown in Figure 5(b), we indeed find that data augmentation improves the BO performance of the translation dependent architecture when trained on the translation invariant PC-A dataset, even matching the performance of a translation invariant architecture on PC-A. However, on the translation dependent PC-B dataset, data augmentation initially hurts the BO performance of the translation dependent architecture because the model is unable to quickly specialize to the more compact distribution of PC-B, putting its BO performance more on par with models trained on PC-A. These results show that techniques used to improve generalization performance (such as data augmentation or invariant architectures) for training deep learning architectures can also be applied to BO surrogate models and, when used appropriately, directly translate into improved BO performance. Note that data augmentation would not be feasible for GPs without a hand-crafted kernel as the increased size of the dataset would cause inference to

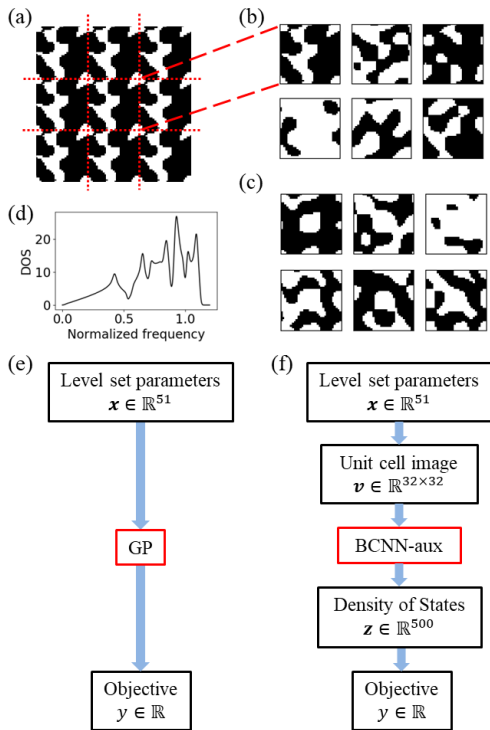


Figure 3. (a) A 2D photonic crystal (PC), where the black and white regions represent different materials, and the periodic unit cells are outlined in red. Examples of PC unit cells drawn from the (b) PC-A distribution where  $c_i \in [-1, 1]$ , and (b) the PC-B distribution which is arbitrarily restricted to  $c_i \in [0, 1]$ . The PC-A data distribution is translation invariant, whereas unit cells drawn from the PC-B distribution all have white regions in the middle of the unit cell, so the distribution is not translation invariant. (d) Example of density of states (DOS) which tell us about the PC’s optical properties. (e, f) Comparison of the process flow for training the surrogate model in the case of (e) GPs and (f) Bayesian Convolutional NNs (BCNN). The BCNN can train directly on the images to take advantage of the structure and symmetries in the data, and predict the multi-dimensional DOS.

become computationally intractable.

### 5.3. Organic Molecule Quantum Chemistry

Finally, we use BO to optimize the chemical properties of molecules. Chemical optimization is of huge interest with applications in drug design and materials optimization (Hughes et al., 2011). This is a difficult problem where computational approaches such as density functional theory (DFT) can take days for simple molecules and are intractable for larger molecules, synthesis is expensive and time-consuming, and the space of synthesizable molecules is huge and complex. There have been many approaches for molecular optimization that largely revolve around finding a continuous latent space of molecules (Gómez-Bombarelli

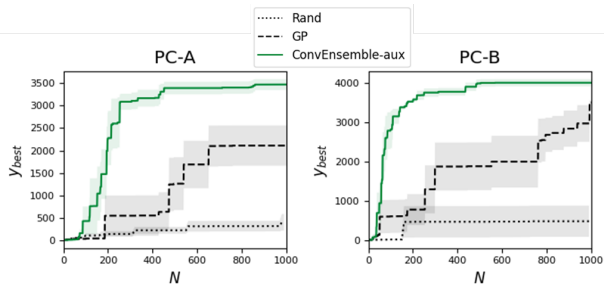


Figure 4. BO results for the (a) PC-A and (b) PC-B datasets. Both ensemble and BBB versions of BCNNs significantly outperform GPs.

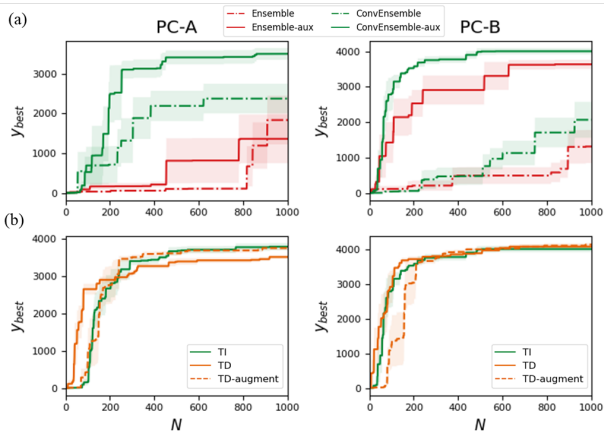


Figure 5. Additional BO results on the photonic crystal dataset demonstrating the effect of model architecture, auxiliary information, and data augmentation. (a) The inductive bias of convolutional layers and the addition of auxiliary information significantly improve performance of BCNNs. (b) Data augmentation boosts performance if the augmentations reflect a symmetry present in the dataset but not enforced by the model architecture. “TI” refers to a translation invariant BCNN architecture, whereas “TD” refers to a translation dependent architecture. “-augment” signifies that data augmentation of the photonic crystal image is applied, which includes periodic translations, flips, and rotations.

et al., 2018) or hand-crafting kernels (Korovina et al., 2020).

Here we focus on the QM9 dataset (Ruddigkeit et al., 2012; Ramakrishnan et al., 2014), which consists of 133,885 small organic molecules along with their geometric, electronic, and thermodynamics quantities that have been calculated with DFT. Instead of optimizing over a continuous space, we draw from the fixed pool of available molecules and iteratively select the next molecule to add to  $\mathcal{D}_{\text{train}}$ .

Graph neural networks (GNNs) are popular for chemistry applications due to the natural encoding of a molecule as a graph with atoms and bonds as nodes and edges. Here we adopt a GNN architecture, implemented by Spektral

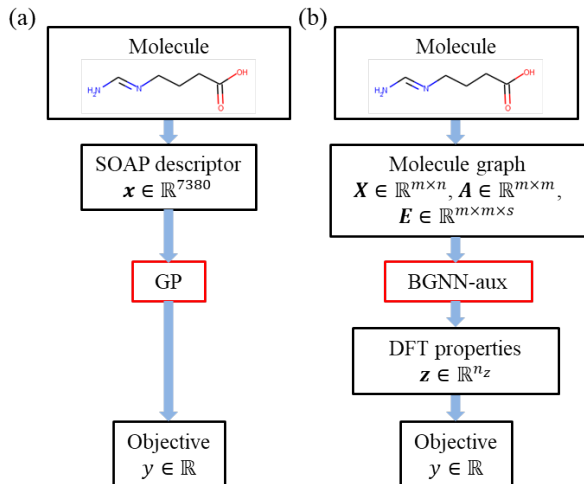


Figure 6. (a) The GP is trained on the SOAP descriptor calculated for each molecule. (b) The BGNN operates directly on a graph representation of the molecule, where atoms and bonds are represented by nodes and edges, respectively. The BGNN can be trained on multiple properties given in the QM9 dataset.

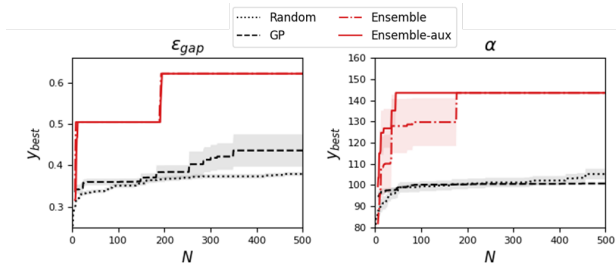


Figure 7. BO results for various properties. For maximizing  $\epsilon_{\text{gap}}$ , the BGNNs quickly reach the maximum value. For maximizing  $\alpha$ , we see that including the extra information significantly improves performance.

(Grattarola & Alippi, 2020), for our Bayesian GNN (BGNN) surrogate model which can be trained directly on molecular graphs, as shown in Figure 6(b). For our GP-based BO baseline, we use the Smooth Overlap of Atomic Positions (SOAP) descriptor to produce a fixed-length feature vector  $\mathbf{x} \in \mathbb{R}^{7380}$  for each molecule, as shown in Figure 6(a) (De et al., 2016; Himanen et al., 2020).

We compare two different optimization objectives provided by the QM9 dataset: the HUMO-LUMO energy gap  $\epsilon_{\text{gap}}$  and the isotropic polarizability  $\alpha$ . Because many of the chemical properties in the QM9 dataset can be collectively computed by a single DFT or molecular dynamics calculation, we can treat a subset of properties from QM9 as auxiliary information  $\mathbf{z}$  and train our BGNN to predict this entire subset simultaneously. The objective function  $h$  then simply picks out the property of interest.

As shown in Figure 7, BGNNs significantly outperform GPs, showing that the inductive bias in the graph structure can lead to a much more natural representation of the molecule and its properties. In the case of maximizing the polarizability  $\alpha$ , including the auxiliary information improves BO performance, showing signs of positive transfer. In the case of maximizing the energy gap  $\epsilon_{\text{gap}}$ , the BGNNs quickly find the maximum value.

## 6. Discussion

The addition of auxiliary information significantly improves the performance of BO for the nanoparticle and photonic crystal tasks. We conjecture that the additional information forces the BNN to learn a more consistent physical model of the system since it must learn features that are shared across the multi-dimensional auxiliary information, thus enabling the BNN to generalize better. For example, the scattering spectrum of the multilayer particle consists of multiple resonances (sharp peaks), the width and location of which are determined by the material properties and layer thicknesses. The BNN could potentially learn these more abstract features, and thus, the deeper physics, to help it interpolate more efficiently as shown in Peurifoy et al. (2018). It is also possible that the loss landscape for the auxiliary information is smoother than that of the objective function and that the auxiliary information acts as an implicit regularization that improves generalization performance.

For the quantum chemistry task, using auxiliary information improves performance for one of the two properties we optimized. This is likely due to the small size of the available auxiliary information (only a handful of chemical properties from the QM dataset) as compared with the other two tasks. In a more realistic online setting, we would have significantly more physically-informative information available from a DFT calculation, e.g. we could easily compute the electronic density of states (the electronic analogue of the auxiliary information used in the photonics task). We also note that deep BO already performs extremely well on the  $\epsilon_{\text{gap}}$  objective function, finding the maximum possible value within a couple hundred iterations, and so there is not much room for improvement.

There is an interesting connection between how well BNNs are able to capture and explore a multi-modal posterior distribution and their performance in BO. For example, we have noticed that larger batch sizes tend to significantly hurt BO performance. On the one hand, larger batch sizes may be resulting in poorer generalization as the model finds sharper local minima in the loss landscape. However, a more likely explanation is that the stochasticity inherent in smaller batch sizes allows the BNN to more easily explore the posterior distribution, which is known to be highly multi-modal (Fort et al., 2019). Indeed, BO often underperforms for very

small dataset sizes  $N$  but quickly catches up as  $N$  increases, indicating that batch size is an important hyperparameter which must be balanced with computational cost.

All our results use continued training (or warm restart) to minimize training costs. We note that re-initializing  $\mathcal{M}$  and training from scratch in every iteration performs better than continued training on some tasks, which points to how BNNs—including ensembles—are not sufficiently capturing a multi-modal posterior distribution. Future work will consider using stochastic training approaches such as SG-MCMC methods for exploring posterior distributions (Welling & Teh, 2011; Zhang et al., 2019b) as well as other continual learning techniques to further minimize training costs, especially for larger datasets (Parisi et al., 2019).

When comparing BNN architectures, we find that ensembles tend to consistently perform among the best, which is supported by previous literature showing that ensembles capture uncertainty much better than variational methods (Ovadia et al., 2019; Gustafsson et al., 2020) especially in multi-modal loss landscapes (Fort et al., 2019). Ensembles are also attractive because they require no additional hyperparameters, and because they are simple to implement and train. Although training costs increase linearly with the size of the ensemble, this can be easily parallelized on modern computing infrastructures. Furthermore, recent work that aim to model efficient ensembles that minimize computational cost could be an interesting future direction (Havasi et al., 2020; Wen et al., 2020).

BBB performs reasonably well and is competitive with or even better than ensembles on some tasks, but it requires significant hyperparameter tuning. Also, the tendency of variational methods such as BBB to underestimate uncertainty is likely detrimental to their performance in BO. Infinitely wide neural networks are another interesting research direction, as the ability to derive infinitely wide versions of various neural network architectures such as convolutions, and more recently graph convolutional layers (Hu et al., 2020) could potentially bring the power of GPs and BO to complex problems in low-data regimes. However, we find they perform relatively poorly, are quite sensitive to hyperparameters (e.g. kernel and parameterization), and current implementations of certain operations such as pooling are too slow for practical use in an iterative setting.

Non-Bayesian global optimization methods such as LIPO and DIRECT-L are quite powerful in spite of their small computational overhead and can even outperform BO on some tasks. However, they are not as consistent as BO, performing more comparably to random sampling on other tasks. CMA-ES performs poorly on all the tasks here. Also, like GPs, these non-Bayesian algorithms assume a continuous input space and cannot be effectively applied to structured, high-dimensional problems.

## 7. Conclusion

We have shown how BNNs can be used as surrogate models in BO, which enables the scaling of BO to large datasets and provides the flexibility to incorporate a wide variety of constraints, data augmentation techniques, and inductive biases. We have demonstrated that integrating domain-knowledge on the structure and symmetries of the data into the surrogate model as well as exploiting intermediate or auxiliary information significantly improves BO performance. Intuitively, providing the BNN surrogate model with all available information allows the BNN to learn a more faithful physical model of the system of interest, thus enhancing the performance of BO. Finally, we have applied BO to real-world, high-dimensional scientific datasets, and our results show that BNNs can outperform GPs.

Future work will investigate more complex BNN architectures with stronger inductive biases. For example, output constraints can be placed through unsupervised learning (Karpatne et al., 2017) or by variationally fitting a BNN prior (Yang et al., 2020). Custom architectures have also been proposed for partial differential equations (Raissi et al., 2017; Lu et al., 2020), many-body systems (Cranmer et al., 2020), and generalized symmetries (Hutchinson et al., 2020), which will enable effective BO on a wider range of tasks. The methods and experiments presented here enable BO to be effectively applied in a wider variety of settings.

## Acknowledgements

The authors would like to acknowledge Rodolphe Jenatton, Thomas Christensen, Andrew Ma, Rumen Dangsovski, Charles Roques-Carnes, and Mohammed Benzaouia for fruitful conversations. The authors acknowledge the MIT SuperCloud and Lincoln Laboratory Supercomputing Center for providing (HPC, database, consultation) resources that have contributed to the research results reported within this paper/report.

This work is supported in part by the the National Science Foundation under Cooperative Agreement PHY-2019786 (The NSF AI Institute for Artificial Intelligence and Fundamental Interactions, <http://iaifi.org/>). This research was also sponsored in part by the Department of Defense through the National Defense Science & Engineering Graduate Fellowship (NDSEG) Program. It is also based upon work supported in part by the U.S. Army Research Office through the Institute for Soldier Nanotechnologies at MIT, under Collaborative Agreement Number W911NF-18-2-0048. Research was sponsored by the United States Air Force Research Laboratory and the United States Air Force Artificial Intelligence Accelerator and was accomplished under Cooperative Agreement Number FA8750-19-2-1000. The views and conclusions contained in this document are



those of the authors and should not be interpreted as representing the official policies, either expressed or implied, of the United States Air Force or the U.S. Government. The U.S. Government is authorized to reproduce and distribute reprints for Government purposes notwithstanding any copyright notation herein.

## References

- Astudillo, R. and Frazier, P. Bayesian optimization of composite functions. In *International Conference on Machine Learning*, pp. 354–363. PMLR, 2019.
- Blundell, C., Cornebise, J., Kavukcuoglu, K., and Wierstra, D. Weight uncertainty in neural networks. *arXiv preprint arXiv:1505.05424*, 2015.
- Brochu, E., Cora, V. M., and De Freitas, N. A tutorial on bayesian optimization of expensive cost functions, with application to active user modeling and hierarchical reinforcement learning. *arXiv preprint arXiv:1012.2599*, 2010.
- Cranmer, M., Sanchez-Gonzalez, A., Battaglia, P., Xu, R., Cranmer, K., Spergel, D., and Ho, S. Discovering symbolic models from deep learning with inductive biases. *arXiv preprint arXiv:2006.11287*, 2020.
- De, S., Bartók, A. P., Csányi, G., and Ceriotti, M. Comparing molecules and solids across structural and alchemical space. *Physical Chemistry Chemical Physics*, 18(20): 13754–13769, 2016.
- Fort, S., Hu, H., and Lakshminarayanan, B. Deep ensembles: A loss landscape perspective. *arXiv preprint arXiv:1912.02757*, 2019.
- Gablonsky, J. M. and Kelley, C. T. A locally-biased form of the direct algorithm. *Journal of Global Optimization*, 21(1):27–37, 2001.
- Gal, Y., Islam, R., and Ghahramani, Z. Deep bayesian active learning with image data. *arXiv preprint arXiv:1703.02910*, 2017.
- Ghosh Chaudhuri, R. and Paria, S. Core/shell nanoparticles: classes, properties, synthesis mechanisms, characterization, and applications. *Chemical reviews*, 112(4): 2373–2433, 2012.
- Gómez-Bombarelli, R., Wei, J. N., Duvenaud, D., Hernández-Lobato, J. M., Sánchez-Lengeling, B., Sheberla, D., Aguilera-Iparraguirre, J., Hirzel, T. D., Adams, R. P., and Aspuru-Guzik, A. Automatic chemical design using a data-driven continuous representation of molecules. *ACS central science*, 4(2):268–276, 2018.
- Grattarola, D. and Alippi, C. Graph neural networks in tensorflow and keras with spektral. *arXiv preprint arXiv:2006.12138*, 2020.
- Griffiths, R.-R. and Hernández-Lobato, J. M. Constrained bayesian optimization for automatic chemical design using variational autoencoders. *Chemical science*, 11(2): 577–586, 2020.
- Gustafsson, F. K., Danelljan, M., and Schon, T. B. Evaluating scalable bayesian deep learning methods for robust computer vision. In *Proceedings of the IEEE/CVF Conference on Computer Vision and Pattern Recognition Workshops*, pp. 318–319, 2020.
- Hansen, N., Akimoto, Y., and Baudis, P. CMA-ES/pycma on Github. Zenodo, DOI:10.5281/zenodo.2559634, February 2019. URL <https://doi.org/10.5281/zenodo.2559634>.
- Havasi, M., Jenatton, R., Fort, S., Liu, J. Z., Snoek, J., Lakshminarayanan, B., Dai, A. M., and Tran, D. Training independent subnetworks for robust prediction. *arXiv preprint arXiv:2010.06610*, 2020.
- Himanen, L., Jäger, M. O. J., Morooka, E. V., Federici Canova, F., Ranawat, Y. S., Gao, D. Z., Rinke, P., and Foster, A. S. Dscribe: Library of descriptors for machine learning in materials science. *Computer Physics Communications*, 247:106949, 2020. ISSN 0010-4655. doi: 10.1016/j.cpc.2019.106949. URL <https://doi.org/10.1016/j.cpc.2019.106949>.
- Ho, C.-I., Yeh, D.-J., Su, V.-C., Yang, C.-H., Yang, P.-C., Pu, M.-Y., Kuan, C.-H., Cheng, I.-C., and Lee, S.-C. Plasmonic multilayer nanoparticles enhanced photocurrent in thin film hydrogenated amorphous silicon solar cells. *Journal of Applied Physics*, 112(2):023113, 2012.
- Hu, J., Shen, J., Yang, B., and Shao, L. Infinitely wide graph convolutional networks: semi-supervised learning via gaussian processes. *arXiv preprint arXiv:2002.12168*, 2020.
- Huang, G., Li, Y., Pleiss, G., Liu, Z., Hopcroft, J. E., and Weinberger, K. Q. Snapshot ensembles: Train 1, get m for free. *arXiv preprint arXiv:1704.00109*, 2017.
- Hughes, J. P., Rees, S., Kalindjian, S. B., and Philpott, K. L. Principles of early drug discovery. *British journal of pharmacology*, 162(6):1239–1249, 2011.
- Hutchinson, M., Lan, C. L., Zaidi, S., Dupont, E., Teh, Y. W., and Kim, H. Lietransformer: Equivariant self-attention for lie groups. *arXiv preprint arXiv:2012.10885*, 2020.

- Hutter, F., Hoos, H. H., and Leyton-Brown, K. Sequential model-based optimization for general algorithm configuration. In *International conference on learning and intelligent optimization*, pp. 507–523. Springer, 2011.
- Jensen, J. S. and Sigmund, O. Topology optimization for nano-photonics. *Laser & Photonics Reviews*, 5(2):308–321, 2011.
- Joannopoulos, J. D., Johnson, S. G., Winn, J. N., and Meade, R. D. *Photonic Crystals: Molding the Flow of Light (Second Edition)*. Princeton University Press, 2 edition, 2008. ISBN 0691124566.
- John, S. Strong localization of photons in certain disordered dielectric superlattices. *Physical review letters*, 58(23): 2486, 1987.
- Johnson, S. G. The nlopt nonlinear-optimization package, 2010. URL <http://github.com/stevengj/nlopt>.
- Jones, D. R., Schonlau, M., and Welch, W. J. Efficient global optimization of expensive black-box functions. *Journal of Global Optimization*, 13(4):455–492, Dec 1998. ISSN 1573-2916. doi: 10.1023/A:1008306431147. URL <https://doi.org/10.1023/A:1008306431147>.
- Karpatne, A., Watkins, W., Read, J., and Kumar, V. Physics-guided neural networks (pgnn): An application in lake temperature modeling. *arXiv preprint arXiv:1710.11431*, 2017.
- King, D. E. Dlib-ml: A machine learning toolkit. *Journal of Machine Learning Research*, 10:1755–1758, 2009.
- Klein, A., Falkner, S., Bartels, S., Hennig, P., and Hutter, F. Fast bayesian optimization of machine learning hyperparameters on large datasets. In *Artificial Intelligence and Statistics*, pp. 528–536. PMLR, 2017.
- Korovina, K., Xu, S., Kandasamy, K., Neiswanger, W., Poczos, B., Schneider, J., and Xing, E. Chembo: Bayesian optimization of small organic molecules with synthesizable recommendations. In *International Conference on Artificial Intelligence and Statistics*, pp. 3393–3403. PMLR, 2020.
- Lakshminarayanan, B., Pritzel, A., and Blundell, C. Simple and scalable predictive uncertainty estimation using deep ensembles. In *Advances in neural information processing systems*, pp. 6402–6413, 2017.
- Lin, Z., Liu, V., Pestourie, R., and Johnson, S. G. Topology optimization of freeform large-area metasurfaces. *Optics express*, 27(11):15765–15775, 2019.
- Loshchilov, I. and Hutter, F. Sgdr: Stochastic gradient descent with warm restarts. *arXiv preprint arXiv:1608.03983*, 2016.
- Louizos, C. and Welling, M. Multiplicative normalizing flows for variational bayesian neural networks. *arXiv preprint arXiv:1703.01961*, 2017.
- Lu, P. Y., Kim, S., and Soljačić, M. Extracting interpretable physical parameters from spatiotemporal systems using unsupervised learning. *Physical Review X*, 10(3):031056, 2020.
- Malherbe, C. and Vayatis, N. Global optimization of lipschitz functions. *arXiv preprint arXiv:1703.02628*, 2017.
- Men, H., Lee, K. Y., Freund, R. M., Peraire, J., and Johnson, S. G. Robust topology optimization of three-dimensional photonic-crystal band-gap structures. *Optics express*, 22(19):22632–22648, 2014.
- Novak, R., Xiao, L., Hron, J., Lee, J., Alemi, A. A., Sohl-Dickstein, J., and Schoenholz, S. S. Neural tangents: Fast and easy infinite neural networks in python. In *International Conference on Learning Representations*, 2020. URL <https://github.com/google/neural-tangents>.
- Ovadia, Y., Fertig, E., Ren, J., Nado, Z., Sculley, D., Nowozin, S., Dillon, J., Lakshminarayanan, B., and Snoek, J. Can you trust your model’s uncertainty? evaluating predictive uncertainty under dataset shift. In *Advances in Neural Information Processing Systems*, pp. 13991–14002, 2019.
- Parisi, G. I., Kemker, R., Part, J. L., Kanan, C., and Wermter, S. Continual lifelong learning with neural networks: A review. *Neural Networks*, 113:54–71, 2019.
- Perrone, V., Jenatton, R., Seeger, M., and Archambeau, C. Scalable hyperparameter transfer learning. In *Proceedings of the 32nd International Conference on Neural Information Processing Systems*, pp. 6846–6856, 2018.
- Peurifoy, J., Shen, Y., Jing, L., Yang, Y., Cano-Renteria, F., DeLacy, B. G., Joannopoulos, J. D., Tegmark, M., and Soljačić, M. Nanophotonic particle simulation and inverse design using artificial neural networks. *Science advances*, 4(6):eaar4206, 2018.
- Piggott, A. Y., Lu, J., Lagoudakis, K. G., Petykiewicz, J., Babinec, T. M., and Vučković, J. Inverse design and demonstration of a compact and broadband on-chip wavelength demultiplexer. *Nature Photonics*, 9(6):374–377, 2015.
- Raissi, M., Perdikaris, P., and Karniadakis, G. E. Physics informed deep learning (part i): Data-driven solutions of

- nonlinear partial differential equations. *arXiv preprint arXiv:1711.10561*, 2017.
- Ramakrishnan, R., Dral, P. O., Rupp, M., and Von Lilienfeld, O. A. Quantum chemistry structures and properties of 134 kilo molecules. *Scientific data*, 1(1):1–7, 2014.
- Riquelme, C., Tucker, G., and Snoek, J. Deep bayesian bandits showdown: An empirical comparison of bayesian deep networks for thompson sampling. *arXiv preprint arXiv:1802.09127*, 2018.
- Ruddigkeit, L., Van Deursen, R., Blum, L. C., and Reymond, J.-L. Enumeration of 166 billion organic small molecules in the chemical universe database gdb-17. *Journal of chemical information and modeling*, 52(11):2864–2875, 2012.
- Saltsberger, S., Steinberg, I., and Gannot, I. Multilayer mie scattering model for investigation of intracellular structural changes in the nucleolus and cytoplasm. *International Journal of Optics*, 2012, 2012.
- Shahriari, B., Swersky, K., Wang, Z., Adams, R. P., and De Freitas, N. Taking the human out of the loop: A review of bayesian optimization. *Proceedings of the IEEE*, 104(1):148–175, 2015.
- Shen, Y., Ye, D., Celanovic, I., Johnson, S. G., Joannopoulos, J. D., and Soljačić, M. Optical broadband angular selectivity. *Science*, 343(6178):1499–1501, 2014.
- Shervashidze, N., Schweitzer, P., Van Leeuwen, E. J., Mehlhorn, K., and Borgwardt, K. M. Weisfeiler-lehman graph kernels. *Journal of Machine Learning Research*, 12(9), 2011.
- Shi, Y., Wang, X., Liu, W., Yang, T., Xu, R., and Yang, F. Multilayer silver nanoparticles for light trapping in thin film solar cells, 2013.
- Siddhant, A. and Lipton, Z. C. Deep bayesian active learning for natural language processing: Results of a large-scale empirical study. *arXiv preprint arXiv:1808.05697*, 2018.
- Snoek, J., Larochelle, H., and Adams, R. P. Practical bayesian optimization of machine learning algorithms. *Advances in neural information processing systems*, 25: 2951–2959, 2012.
- Snoek, J., Rippel, O., Swersky, K., Kiros, R., Satish, N., Sundaram, N., Patwary, M., Prabhat, M., and Adams, R. Scalable bayesian optimization using deep neural networks. In *International conference on machine learning*, pp. 2171–2180, 2015.
- Springenberg, J. T., Klein, A., Falkner, S., and Hutter, F. Bayesian optimization with robust bayesian neural networks. *Advances in neural information processing systems*, 29:4134–4142, 2016.
- Swersky, K., Snoek, J., and Adams, R. P. Freeze-thaw bayesian optimization. *arXiv preprint arXiv:1406.3896*, 2014.
- Tang, W. and Henkelman, G. Charge redistribution in core-shell nanoparticles to promote oxygen reduction. *The Journal of chemical physics*, 130(19):194504, 2009.
- The GPyOpt authors. GPyOpt: A bayesian optimization framework in python. <http://github.com/SheffieldML/GPyOpt>, 2016.
- Ueno, T., Rhone, T. D., Hou, Z., Mizoguchi, T., and Tsuda, K. Combo: an efficient bayesian optimization library for materials science. *Materials discovery*, 4:18–21, 2016.
- Van der Wilk, M., Rasmussen, C. E., and Hensman, J. Convolutional gaussian processes. *arXiv preprint arXiv:1709.01894*, 2017.
- Walker, I. and Glocker, B. Graph convolutional gaussian processes. In *International Conference on Machine Learning*, pp. 6495–6504. PMLR, 2019.
- Welling, M. and Teh, Y. W. Bayesian learning via stochastic gradient langevin dynamics. In *Proceedings of the 28th international conference on machine learning (ICML-11)*, pp. 681–688, 2011.
- Wen, Y., Tran, D., and Ba, J. Batchensemble: an alternative approach to efficient ensemble and lifelong learning. *arXiv preprint arXiv:2002.06715*, 2020.
- Wilson, A. G., Hu, Z., Salakhutdinov, R., and Xing, E. P. Deep kernel learning. In *Artificial intelligence and statistics*, pp. 370–378. PMLR, 2016.
- Yablonovitch, E. Inhibited spontaneous emission in solid-state physics and electronics. *Physical review letters*, 58(20):2059, 1987.
- Yang, W., Lorch, L., Graule, M. A., Lakkaraju, H., and Doshi-Velez, F. Incorporating interpretable output constraints in bayesian neural networks. *arXiv preprint arXiv:2010.10969*, 2020.
- Zhang, D., Lu, L., Guo, L., and Karniadakis, G. E. Quantifying total uncertainty in physics-informed neural networks for solving forward and inverse stochastic problems. *Journal of Computational Physics*, 397:108850, 2019a.
- Zhang, R., Li, C., Zhang, J., Chen, C., and Wilson, A. G. Cyclical stochastic gradient mcmc for bayesian deep learning. *arXiv preprint arXiv:1902.03932*, 2019b.

# Scalable and Flexible Deep Bayesian Optimization with Auxiliary Information for Scientific Problems: Supplementary Material

Samuel Kim<sup>1</sup> Peter Y. Lu<sup>2</sup> Charlotte Loh<sup>1</sup> Jamie Smith<sup>3</sup> Jasper Snoek<sup>3</sup> Marin Soljačić<sup>2</sup>

## 1. Datasets

### 1.1. Nanoparticle Scattering

The multilayer nanoparticle consists of a lossless silica core surrounded by alternating layers of lossless TiO<sub>2</sub> and lossless silica. The relative permittivity of silica is  $\varepsilon_{\text{silica}} = 2.04$ . The relative permittivity of TiO<sub>2</sub> is dispersive and depends on the wavelength of light:

$$\varepsilon_{\text{TiO}_2} = 5.913 + \frac{0.2441}{10^{-6}\lambda^2 - 0.0803} \quad (1)$$

where  $\lambda$  is the wavelength given in units of nm. The entire particle is surrounded by water, which has a relative permittivity of  $\varepsilon_{\text{water}} = 1.77$ .

For a given set of thicknesses, we analytically solve for the scattering spectrum, i.e. the scattering cross-section  $\sigma(\lambda)$  as a function of wavelength  $\lambda$ , using Mie scattering as described in [Qiu et al. \(2012\)](#). The code for computing  $\sigma$  was adapted from [Peurifoy et al. \(2018\)](#).

The objective functions for the narrowband and highpass objectives are given as:

$$h_{\text{nb}}(\mathbf{z}) = \frac{\int_{\lambda \in \text{nb}} \sigma(\lambda) d\lambda}{\int_{\text{elsewhere}} \sigma(\lambda) d\lambda} \approx \frac{\sum_{i=126}^{145} z_i}{\sum_{i=1}^{125} z_i + \sum_{i=146}^{201} z_i} \quad (2)$$

$$h_{\text{hp}}(\mathbf{z}) = \frac{\int_{\lambda \in \text{hp}} \sigma(\lambda) d\lambda}{\int_{\text{elsewhere}} \sigma(\lambda) d\lambda} \approx \frac{\sum_{i=126}^{201} z_i}{\sum_{i=1}^{125} z_i}, \quad (3)$$

where  $\mathbf{z} \in \mathbb{R}^{201}$  is the discretized scattering cross-section  $\sigma(\lambda)$  from  $\lambda = 350$  nm to 750 nm.

### 1.2. Photonic Crystal

The photonic crystal (PC) consists of periodic unit cells with periodicity  $a = 1$   $\mu\text{m}$ , where each unit cell is depicted

as a “two-tone” image, with the white regions representing silicon with permittivity  $\varepsilon_1 = 11.4$  and black regions representing vacuum (or air) with permittivity  $\varepsilon_0 = 1$ .

The photonic crystal (PC) structure is defined by a spatially varying permittivity  $\varepsilon(x, y) \in \{\varepsilon_0, \varepsilon_1\}$  over a 2D periodic unit cell with spatial coordinates  $x, y \in [0, a]$ . To parameterize  $\varepsilon$ , we choose a level set of a Fourier sum function  $\phi$ , defined as a linear combination of plane waves with frequencies evenly spaced in the reciprocal lattice space up to a maximum cutoff. Intuitively, the upper limit on the frequencies roughly corresponds to a lower limit on the feature size such that the photonic crystal remains within reasonable fabrication constraints. Here we set the cutoff such that there are 25 complex frequencies corresponding to 50 real coefficients  $\mathbf{c} = (c_1, c_2, \dots, c_{50})$ .

Explicitly, we have

$$\phi[\mathbf{c}](x, y) = \text{Re} \left\{ \sum_{k=1}^{25} (c_k + i c_{k+25}) e^{2\pi i (n_x x + n_y y)/a} \right\}, \quad (4)$$

where each exponential term is composed from the 25 different pairs  $\{n_x, n_y\}$  with  $n_x, n_y \in [-2, -1, 0, 1, 2]$ . We then choose a level-set offset  $\Delta$  to determine the PC structure, where regions with  $\phi > \Delta$  are assigned to be silicon and regions where  $\phi \leq \Delta$  are vacuum. Thus, the photonic crystal unit cell topology is parameterized by a 51-dimensional vector,  $[c_1, c_2, \dots, c_{50}, \Delta]^T \in \mathbb{R}^{51}$ . More specifically,

$$\varepsilon(x, y) = \varepsilon[\mathbf{c}, \Delta](x, y) = \begin{cases} \varepsilon_1 & \phi[\mathbf{c}](x, y) > \Delta \\ \varepsilon_0 & \phi[\mathbf{c}](x, y) \leq \Delta \end{cases}, \quad (5)$$

which is discretized to result in a  $32 \times 32$  pixel image  $\mathbf{v} \in \{\varepsilon_0, \varepsilon_1\}^{32 \times 32}$ . This formulation also has the advantage of enforcing periodic boundary conditions.

For each unit cell, we use the MIT Photonics Bands (MPB) software ([Johnson & Joannopoulos, 2001](#)) to compute the band structure of the photonic crystal,  $\omega(\mathbf{k})$ , up to the lowest 10 bands, using a  $32 \times 32$  spatial resolution (or equivalently,  $32 \times 32$  k-points over the Brillouin zone  $-\frac{\pi}{a} < k < \frac{\pi}{a}$ ). We also extract the group velocities at each k-point and compute the density-of-states (DOS) via an extrapolative

<sup>1</sup>Department of Electrical Engineering and Computer Science, Massachusetts Institute of Technology, Cambridge, Massachusetts, USA <sup>2</sup>Department of Physics, Massachusetts Institute of Technology, Cambridge, Massachusetts, USA <sup>3</sup>Google Research, Cambridge, Massachusetts, USA. Correspondence to: Samuel Kim <samkim@mit.edu>.



technique, adapted from Liu et al. (2018). The DOS is computed at a resolution of 20,000 points, and a Gaussian filter of kernel size 100 is used to smooth the DOS spectrum. To normalize the frequency scale across the different unit cells, the frequency is rescaled via  $\omega\sqrt{\epsilon_{avg}} \rightarrow \omega_{norm}$ , where  $\epsilon_{avg} = \frac{1}{a^2} \int_0^a \int_0^a \epsilon(x, y) dx dy \approx \frac{1}{(32)^2} \sum_{i,j} v_{i,j}$  is the average permittivity over all pixels. Finally, the DOS spectrum is truncated at  $\omega_{norm} = 1.2$  and interpolated using 500 points to give  $\mathbf{z} \in \mathbb{R}^{500}$ .

The objective function aims to minimize the DOS in a small frequency range and maximize it elsewhere. We use the following:

$$h_{\text{DOS}}(\mathbf{z}) = \frac{\sum_{i=1}^{300} z_i + \sum_{i=351}^{500} z_i}{1 + \sum_{i=301}^{350} z_i}, \quad (6)$$

where the 1 is added in the denominator to avoid singular values.

### 1.3. Organic Molecule Quantum Chemistry

The Smooth Overlap of Atomic Positions (SOAP) descriptor (De et al., 2016) uses smoothed atomic densities to describe local environments for each atom in the molecule through a fixed-length feature vector, which can then be averaged over all the atoms in the molecule to produce a fixed-length feature vector for the molecule. This descriptor is invariant to translations, rotations, and permutations. We use the SOAP descriptor implemented by DScribe (Himanen et al., 2020) using the recommended parameters: local cut-off `rcut` = 5, number of radial basis functions `nmax` = 8, and maximum degree of spherical harmonics `lmax` = 8. We use `outer` averaging, which averages over the power spectrum of different sites.

The graph representation of each molecule is processed by the Spektral package (Grattarola & Alippi, 2020). Each graph is represented by a node feature matrix  $\mathbf{X} \in \mathbb{R}^{s \times d_n}$ , an adjacency matrix  $\mathbf{A} \in \mathbb{R}^{s \times s}$ , and an edge matrix  $\mathbf{E} \in \mathbb{R}^{e \times d_e}$ , where  $s$  is the number of atoms in the molecule,  $e$  is the number of bonds, and  $d_n, d_e$  are the number of features for nodes and edges, respectively.

The properties that we use from the QM9 dataset are listed in Table 1. We separate these properties into two categories: (1) the *ground state quantities* which are calculated from a single DFT calculation of the molecule and include geometric, energetic, and electronic quantities, and (2) the *thermodynamic quantities* which are typically calculated from a molecular dynamics simulation.

The auxiliary information for this task consist of the properties listed in Table 1 that are in the same category as the objective property, as these properties would be calculated together. The objective function then simply picks out the corresponding feature from the auxiliary information. More

Table 1. List of properties from the QM9 dataset used as labels

PROPERTY	UNIT	DESCRIPTION
<i>Ground State Quantities</i>		
$A$	GHz	ROTATIONAL CONSTANT
$B$	GHz	ROTATIONAL CONSTANT
$C$	GHz	ROTATIONAL CONSTANT
$\mu$	D	DIPOLE MOMENT
$\alpha$	$a_0^3$	ISOTROPIC POLARIZABILITY
$\epsilon_{\text{HOMO}}$	Ha	ENERGY OF HOMO
$\epsilon_{\text{LUMO}}$	Ha	ENERGY OF LUMO
$\epsilon_{\text{GAP}}$	Ha	GAP ( $\epsilon_{\text{LUMO}} - \epsilon_{\text{HOMO}}$ )
$\langle R^2 \rangle$	$a_0^2$	ELECTRONIC SPATIAL EXTENT
<i>Thermodynamic Quantities at 298.15 K</i>		
$U$	Ha	INTERNAL ENERGY
$H$	Ha	ENTHALPY
$G$	Ha	FREE ENERGY
$C_V$	$\frac{\text{cal}}{\text{mol K}}$	HEAT CAPACITY

precisely, for the ground state objectives, the auxiliary information is

$$\mathbf{z} = [A, B, C, \mu, \alpha, \epsilon_{\text{HOMO}}, \epsilon_{\text{LUMO}}, \epsilon_{\text{gap}}, \langle R^2 \rangle] \in \mathbb{R}^9, \quad (7)$$

and the objective functions are

$$h_{\epsilon_{\text{gap}}}(\mathbf{z}) = z_8 \quad (8)$$

$$h_{-\epsilon_{\text{gap}}}(\mathbf{z}) = -z_8 \quad (9)$$

$$h_{\alpha}(\mathbf{z}) = z_5. \quad (10)$$

For thermodynamic objective  $C_V$ , the auxiliary information is

$$\mathbf{z} = [U, H, G, C_V] \in \mathbb{R}^4, \quad (11)$$

and the objective function is

$$h_{C_V}(\mathbf{z}) = z_4. \quad (12)$$

## 2. Bayesian Optimization

**Algorithm 1** Bayesian optimization with auxiliary information

- 1: **Input:** Labelled dataset  $\mathcal{D}_{\text{train}} = \{(\mathbf{x}_n, \mathbf{z}_n, y_n)\}_{n=1}^{N_{\text{start}}=5}$
- 2: **for**  $N = 5$  **to** 1000 **do**
- 3:   Train  $\mathcal{M}: \mathcal{X} \rightarrow \mathcal{Z}$  on  $\mathcal{D}_{\text{train}}$
- 4:   Form an unlabelled dataset,  $\mathcal{X}_{\text{pool}}$
- 5:   Find  $\mathbf{x}_{N+1} = \arg \max_{\mathbf{x} \in \mathcal{X}_{\text{pool}}} \alpha(\mathbf{x}; \mathcal{M}, \mathcal{D}_{\text{train}})$
- 6:   Label the data  $\mathbf{z}_{N+1} = g(\mathbf{x}_{N+1})$ ,  $y_{N+1} = h(\mathbf{z}_{N+1})$
- 7:    $\mathcal{D}_{\text{train}} = \mathcal{D}_{\text{train}} \cup (\mathbf{x}_{N+1}, \mathbf{z}_{N+1}, y_{N+1})$
- 8: **end for**

Our algorithm for Bayesian optimization using auxiliary information  $\mathbf{z}$  is shown in Algorithm 1. This algorithm reduces to the basic BO algorithm in the case where  $h$  is

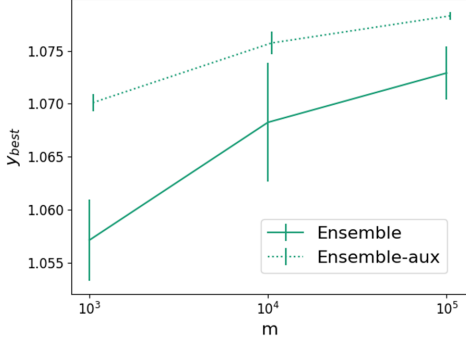


Figure 1. Effect of  $|\mathcal{X}_{\text{pool}}|$  used in the inner optimization loop to maximize the acquisition function on overall BO performance.  $y_{\text{best}}$  is taken from the highpass objective function using the ensemble architecture, where “aux” denotes using auxiliary information.

the identity function and  $\mathcal{Z} = \mathcal{Y}$  such that we can ignore mention of  $\mathbf{z}$  in Algorithm 1.

As mentioned in the main text, the inner optimization loop in line 5 of Algorithm 1 is performed by finding the maximum value of  $\alpha$  over a pool of  $|\mathcal{X}_{\text{pool}}|$  randomly sampled points. We can see in Figure 1 that increasing  $|\mathcal{X}_{\text{pool}}|$  in the acquisition step tends to improve BO performance. Thus, there is likely further room for improvement of the inner optimization loop using more sophisticated algorithms, possibly using the gradient information provided by BNNs.

### 3. Models and Hyperparameters

All BNNs other than the infinitely-wide networks are implemented in TensorFlow v1. Models are trained using the Adam optimizer using the cosine annealing learning rate with a base learning rate of  $10^{-3}$  Loshchilov & Hutter (2016). All hidden layers use ReLU as the activation function, and no activation function is applied to the output layer.

Infinite-width neural networks are implemented using the Neural Tangents library (Novak et al., 2020). We use two different types of infinite networks: (1) “GP-” refers to a closed form expression for Gaussian process inference using the neural network as a kernel, and (2) “INF-” refers to an infinite ensemble of infinite-width networks that have been “trained” with continuous gradient descent for an infinite time. We compare NNGP and NTK kernels as well as the parameterization of the layers. By default, we use the NTK parameterization, but we also use the standard parameterization, denoted by “-STD”.

We also experiment with KL annealing in BBB, a proposed method to improve the performance of variational methods for BNNs in which the weight of the KL term in the loss

function is slowly increased throughout training (Wenzel et al., 2020). For these experiments, we exponentially anneal the KL term with weight  $\sigma_{KL}(i) = 10^{i/500-5}$  as a function of epoch  $i$  when training from scratch; during the continued training, the weight is held constant at  $\sigma_{KL} = 10^{-3}$ .

Task-specific architecture details are listed in Section 4.

## 4. Additional Results

### 4.1. Test Functions

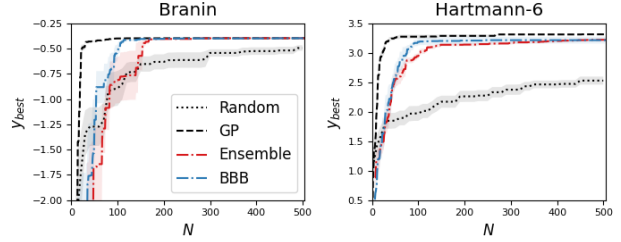


Figure 2. BO results for the Branin and Hartmann-6 functions.

We test BO on several common synthetic functions used for optimization, namely the Branin and 6-dimensional Hartmann functions. We use BNNs with 4 hidden layers and 256 units in each hidden layer, where each hidden layer is followed by a ReLU activation function. Plots of the best value  $y_{\text{best}}$  at each BO iteration are shown in Figure 2. As expected, GPs perform the best. Ensembles and BBB also perform competitively and much better than random sampling, showing that deep BO is viable even for low-dimensional black-box functions.

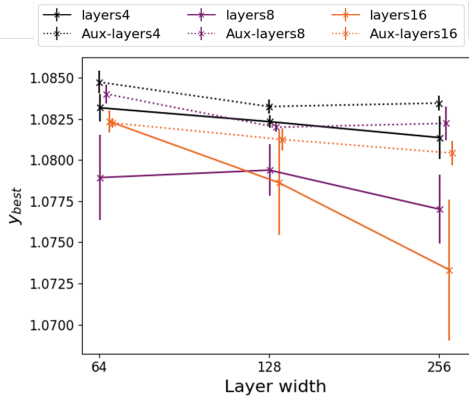
### 4.2. Nanoparticle Scattering

Unless stated otherwise, all the BNNs used for the nanoparticle scattering problem use an architecture consisting of 8 hidden layers with 256 units each. The infinite-width neural networks for the nanoparticle task consist of 8 hidden layers of infinite width, each of which are followed by ReLU activation functions. Detailed BO results for the nanoparticle scattering problem are shown in Table 2.

KL annealing in the BBB architecture significantly improves performance for the narrowband objective, although results are mixed for the highpass objective. Additionally, KL annealing has the downside of introducing more parameters that must be carefully tuned for optimal performance. MNF performs poorly, especially on the highpass objective where it is comparable to random sampling, and we have found that MNF is quite sensitive to the choice of hyperparameters for uncertainty estimates even on simple regression problems. The different variants infinite-width neural networks do not perform as well as the BNNs on both objective functions,

Table 2. BO results for the nanoparticle scattering problem. \* denotes that  $y_{\text{best}}$  is measured at  $N = 50$  due to computational constraints

MODEL	NARROWBAND				HIGHPASS			
	$y_{\text{BEST}}$ AT $N = 250$		$y_{\text{BEST}}$ AT $N = 1000$		$y_{\text{BEST}}$ AT $N = 250$		$y_{\text{BEST}}$ AT $N = 100$	
	MEAN	SE	MEAN	SE	MEAN	SE	MEAN	SE
GP	0.1606	0.0005	0.1621	0.0001	1.0839	0.0017	1.0851	0.0008
GP-AUX	*0.1447	0.0029	-	-	*0.9249	0.0212	-	-
ENSEMBLE	0.1558	0.0011	0.1607	0.0003	1.0729	0.0025	1.077	0.0021
ENSEMBLE-AUX	0.1578	0.0014	0.1593	0.0013	1.0783	0.0003	1.0822	0.001
BBB	0.1596	0.0006	0.1596	0.0006	1.0753	0.0005	1.0753	0.0005
BBB-AUX	0.1601	0.001	0.1601	0.001	1.076	0.0028	1.076	0.0028
BBB-ANNEAL	0.1598	0.001	0.1611	0.0001	1.0813	0.0003	1.0821	0.0005
BBB-AUX-ANNEAL	0.1613	0.0003	0.1619	0	1.0826	0.0008	1.0834	0.0005
MNF	0.15	0.0005	0.1547	0.0004	1.027	0.005	1.0312	0.0036
MNF-AUX	0.1549	0.0014	0.1569	0.0006	0.9957	0.0168	1.028	0.0157
NEURAL LINEAR	0.1543	0.002	0.1579	0.0015	1.0798	0.0007	1.0836	0.0007
INF-NNGP	0.1541	0.0011	0.157	0.0009	1.055	0.0036	1.0653	0.0022
INF-NTK	0.1536	0.0008	0.1571	0.001	1.041	0.004	1.0612	0.0011
INF-NNGP-STD	0.1551	0.0006	0.1598	0.0006	1.0615	0.0043	1.069	0.0018
INF-NTK-STD	0.1564	0.0006	0.1607	0.0001	1.0607	0.0039	1.0761	0.0014
GP-NNGP	0.1582	0.0007	0.1609	0.0001	1.0621	0.0027	1.0694	0.0019
GP-NTK	0.1573	0.001	0.1611	0.0001	1.0667	0.0032	1.0732	0.0012
GP-NNGP-STD	0.1562	0.0008	0.1595	0.001	1.0615	0.0058	1.0718	0.0024
GP-NTK-STD	0.1592	0.0011	0.1608	0.0002	1.0641	0.0033	1.0704	0.0017
RANDOM	0.1527	0.0008	0.1555	0.0006	1.0053	0.0063	1.0362	0.0047
LIPO	0.1604	0.0016	0.1619	0.0006	1.0792	0.0066	1.087	0.0034
DIRECT-L	0.1544	0	0.156	0	1.0777	0	1.0801	0
CMA	0.1424	0.0046	0.143	0.0048	1.059	0.0117	1.076	0.0127


 Figure 3. Comparison of  $y_{\text{best}}$  at  $N = 1000$  for the nanoparticle narrowband objective function for a variety of neural network sizes. All results are ensembles, and “aux” denotes using auxiliary information.

despite the hyper-parameter search.

LIPO seems to perform as well as GPs on both objective functions, which is impressive given the computational speed of the LIPO algorithm. Interestingly DIRECT-L does not perform as well as LIPO or GPs on the narrowband objective, and actually performs comparably to random sampling on the highpass objective. Additionally, CMA performs poorly on both objectives, likely due to the highly

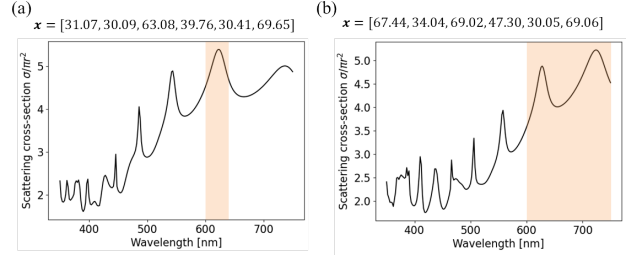


Figure 4. Examples of optimized nanoparticles and their scattering spectrum using the “ENSEMBLE-AUX” architecture for the (a) narrowband and (c) highpass objectives. Orange shaded regions mark the range over which we wish to maximize the scattering. All results were optimized by the “ensemble-aux” architecture.

multimodal nature of the objective function landscape.

We also look at the effect of model size in terms of number of layers and units in Figure 3 for ensembles. While including auxiliary information clearly improves performance across all architectures, there is not a clear trend of performance with respect to the model size. Thus, the performance of BO seems to be somewhat robust to the exact architecture as long as the model is large enough to accurately and efficiently train on the data.

Examples of the optimized structures by the “ENSEMBLE-AUX” architecture are shown in Figure 4. We can see that

the scattering spectra peak in the shaded region of interest, as desired by the respective objective functions.

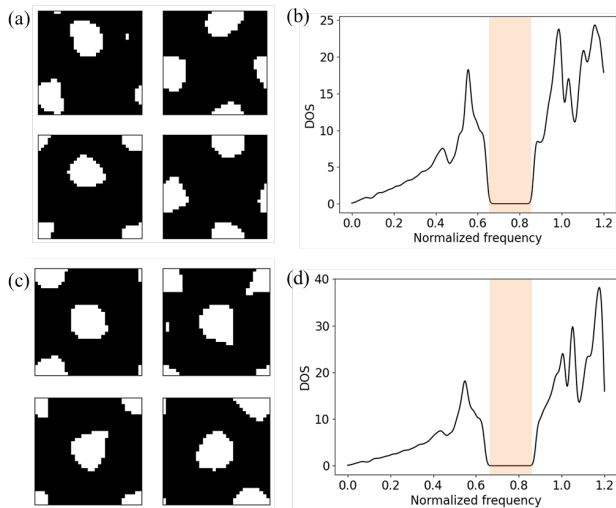


Figure 5. Examples of optimized photonic crystal unit cells over multiple trials for (a) PC-A distribution and (c) PC-B distribution. (b,d) Examples of the optimized DOS. Note that the DOS has been minimized to nearly zero in a thin frequency range. Orange shaded regions mark the frequency range in which we wish to minimize the DOS. All results were optimized by the “ENSEMBLE-AUX” architecture.

### 4.3. Photonic Crystal

The BNN and BCNN architectures that we use for the PC task are listed in Table 3. The size of the “FC” architectures are chosen to have a similar number of parameters as their convolutional counterparts. Unless otherwise stated, all results in the main text and here use the “CONV-TI” and “FC” architectures for BCNNs and BNNs, respectively.

The infinite-width convolutional neural networks (which act as convolutional kernels for GPs) in the PC task consist of 5 convolutional layers followed by 4 fully-connected layers of infinite width. Because the pooling layers in the Neural Tangents library are currently too slow for use in application, we increased the size of the filters to  $5 \times 5$  to increase the receptive field of each filter.

Detailed BO results for the PC problem are shown in Table 4. For algorithms that optimize over the level set parameterization  $\mathbb{R}^{51}$ , we see that GPs perform consistently well, although BNNs using auxiliary information (e.g. Ensemble-Aux) can outperform GPs. DIRECT-L and CMA perform extremely well on the PC-A distribution but performs worse than GP on the PC-B distribution.

Adding convolutional layers and auxiliary information improves performance such that BCNNs significantly outperform GPs. Interestingly, the infinite-width networks perform

extremely poorly, although this may be due to a lack of pooling layers in their architecture which limits the receptive field of the convolutions.

Examples of the optimized structures by the “ENSEMBLE-AUX” architecture are shown in Figure 5. The photonic crystal unit cells generally converged to the same shape: a square lattice of silicon posts with periodicity  $\sqrt{2}a$ .

### 4.4. Organic Molecule Quantum Chemistry

The Bayesian graph neural networks (BGNNs) used for the chemical property optimization task consist of 4 edge-conditioned graph convolutional layers with 32 channels each, followed by a global average pooling operation, followed by 4 fully-connected hidden layers of 64 units each. The edge-conditioned graph convolutional layers (Simonovsky & Komodakis, 2017) are implemented by Spektral (Grattarola & Alippi, 2020).

More detailed results for the quantum chemistry dataset are shown in Table 5. The architecture with the Bayes by Backprop variational approximation applied to every layer (“BBB”), including the graph convolutional layers, performs extremely poorly, even worse than random sampling in some cases. However, only making the fully-connected layers Bayesian (“BBB-FC”) performs surprisingly well.

Ensembles trained with auxiliary information (“ENSEMBLE-AUX”) and neural linear (“NEURALLINEAR”) perform the best on all objective functions. Adding auxiliary information to ensembles helps for the  $\alpha$  objective function, and neither helps nor hurts for the other objective functions. Additionally, BNNs perform at least as well or significantly better than GPs in all cases.

## References

- De, S., Bartók, A. P., Csányi, G., and Ceriotti, M. Comparing molecules and solids across structural and alchemical space. *Physical Chemistry Chemical Physics*, 18(20): 13754–13769, 2016.
- Grattarola, D. and Alippi, C. Graph neural networks in tensorflow and keras with spektral. *arXiv preprint arXiv:2006.12138*, 2020.
- Himanen, L., Jäger, M. O. J., Morooka, E. V., Federici Canova, F., Ranawat, Y. S., Gao, D. Z., Rinke, P., and Foster, A. S. Dscribe: Library of descriptors for machine learning in materials science. *Computer Physics Communications*, 247:106949, 2020. ISSN 0010-4655. doi: 10.1016/j.cpc.2019.106949. URL <https://doi.org/10.1016/j.cpc.2019.106949>.
- Johnson, S. G. and Joannopoulos, J. D. Block-iterative



Table 3. Various architectures for BNNs and BCNNs used in the PC problem. Numbers represent the number of channels and units for the convolutional and fully-connected layers, respectively. All convolutional layers use  $3 \times 3$ -sized filters with stride (1, 1) and periodic boundaries. “MP” denotes max-pooling layers of size  $2 \times 2$  with stride (2, 2), and “AP” denotes average-pooling layers of size  $2 \times 2$  with stride (1, 1). “CONV” denotes BCNNs whereas “FC” denotes BNNs (containing only fully-connected layers) that act on the level-set parameterization  $\mathbf{x}$  rather than on the image  $\mathbf{v}$ . “TI” denotes translation invariant architectures, whereas “TD” denotes translation dependent architectures (i.e. not translation invariant).

ARCHITECTURE	CONVOLUTIONAL LAYERS	FULLY-CONNECTED LAYERS
CONV-TI	16-MP-32-MP-64-MP-128-MP-256	256-256-256-256
CONV-TD	8-AP-8-MP-16-AP-32-MP-32-AP	256-256-256-256
FC	n/a	256-256-256-256-256

Table 4. Select BO results for the PC problem. \* denotes that  $y_{\text{best}}$  is measured at  $N = 750$  as computational constraints made it difficult to reach  $N = 1000$  across all trials.

MODEL	PC-A				PC-B			
	$y_{\text{BEST}}$ AT $N = 250$		$y_{\text{BEST}}$ AT $N = 1000$		$y_{\text{BEST}}$ AT $N = 250$		$y_{\text{BEST}}$ AT $N = 100$	
	MEAN	SE	MEAN	SE	MEAN	SE	MEAN	SE
GP	548	450	2109	448	781	394	3502	49
ENSEMBLE	30	2	841	448	216	145	1318	465
ENSEMBLE-AUX	305	217	1310	509	2909	408	3633	130
CONVENSEMBLE	1140	471	2375	371	390	263	2070	505
CONVENSEMBLE-AUX	2623	558	3468	120	3752	106	4002	92
BBB	75	31	350	207	704	502	780	485
BBB-AUX	39	7	413	313	554	371	1605	544
CONVBBC	712	416	1486	490	928	600	930	599
CONVBBC-AUX	2109	583	3124	43	1761	724	1928	711
NEURALLINEAR	1009	549	1235	481	685	488	2853	291
CONVNEURALLINEAR	1160	540	2524	479	1643	596	2722	647
CONV-INF-NNGP	29	8	322	181	21	7	157	42
CONV-INF-NTK	49	32	425	322	28	7	907	711
CONV-GP-NNGP	15	2	221	118	37	5	830	533
CONV-GP-NTK	20	10	194	139	34	12	85	45
CONV-INF-NNGP-STD	17	3	732	432	66	15	889	442
CONV-INF-NTK-STD	52	31	99	64	8	0	27	12
CONV-GP-NNGP-STD	20	7	*101	59	100	55	*124	49
CONV-GP-NTK-STD	13	5	*132	77	7	0	*686	575
RANDOM	141	61	402	184	471	398	485	395
LIPO	940	1073	1280	1073	1837	1792	2266	1626
DIRECT-L	20	0	4351	1	8	0	2525	38
CMA	9	1	4078	126	10	3	1777	969

frequency-domain methods for maxwell’s equations in a planewave basis. *Optics express*, 8(3):173–190, 2001.

Liu, B., Johnson, S. G., Joannopoulos, J. D., and Lu, L. Generalized gilat-raubenheimer method for density-of-states calculation in photonic crystals. *Journal of Optics*, 20(4):044005, 2018.

Loshchilov, I. and Hutter, F. Sgdr: Stochastic gradient descent with warm restarts. *arXiv preprint arXiv:1608.03983*, 2016.

Novak, R., Xiao, L., Hron, J., Lee, J., Alemi, A. A., Sohl-Dickstein, J., and Schoenholz, S. S. Neural tangents: Fast and easy infinite neural networks in python. In *International Conference on Learning Representa-*

tions, 2020. URL <https://github.com/google/neural-tangents>.

Peurifoy, J., Shen, Y., Jing, L., Yang, Y., Cano-Renteria, F., DeLacy, B. G., Joannopoulos, J. D., Tegmark, M., and Soljačić, M. Nanophotonic particle simulation and inverse design using artificial neural networks. *Science advances*, 4(6):eaar4206, 2018.

Qiu, W., DeLacy, B. G., Johnson, S. G., Joannopoulos, J. D., and Soljačić, M. Optimization of broadband optical response of multilayer nanospheres. *Optics express*, 20(16):18494–18504, 2012.

Simonovsky, M. and Komodakis, N. Dynamic edge-conditioned filters in convolutional neural networks on

Table 5. BO results for the four different quantum chemistry objective functions

MODEL	$y_{\text{BEST}}$ AT $N = 500$							
	$\epsilon_{\text{GAP}}$		$-\epsilon_{\text{GAP}}$		$\alpha$		$C_V$	
	MEAN	SD	MEAN	SD	MEAN	SD	MEAN	SD
GP	0.44	0.11	-0.1	0.02	100.73	1.5	46.68	0.78
GRAPHENSEMBLE	0.62	0	-0.1	0	143.53	0	46.97	0
GRAPHENSEMBLE-AUX	0.62	0	-0.1	0	143.53	0	46.97	0
GRAPHBBB	0.38	0.01	-0.11	0.01	94.46	1.16	41.43	1.58
GRAPHBBB-FC	0.62	0	-0.1	0	135.64	13.67	46.97	0
GRAPHNEURALLINEAR	0.62	0	-0.09	0.01	143.53	0	46.97	0
RANDOM	0.38	0.02	-0.11	0.03	105.19	7.87	43.33	1.25

graphs. In *Proceedings of the IEEE conference on computer vision and pattern recognition*, pp. 3693–3702, 2017.

Wenzel, F., Roth, K., Veeling, B. S., Świątkowski, J., Tran, L., Mandt, S., Snoek, J., Salimans, T., Jenatton, R., and Nowozin, S. How good is the bayes posterior in deep neural networks really? *arXiv preprint arXiv:2002.02405*, 2020.